Polymer Chemistry

Unraveling the kinetics of the structural development during polymerization-induced self-assembly: Decoupling the polymerization and the micelle structure

Journal:	*Polymer Chemistry*
Manuscript ID	PY-ART-11-2019-001810.R1
Article Type:	Paper
Date Submitted by the Author:	25-Dec-2019
Complete List of Authors:	Takahashi, Rintaro; University of Kitakyushu, Department of Chemistry and Biochemistry Miwa, Shotaro; The University of Kitakyushu, Sobotta, Fabian; Friedrich-Schiller-Universitat Jena, Lee, Ji Ha; University of Kitakyushu, Department of Chemistry and Biochemistry Fujii, Shota; University of Kitakyushu, Ohta, Noboru; JASRI/SPring-8, Brendel, Johannes; Friedrich-Schiller-Universitat Jena, Jena Center for Soft Matter Sakurai, Kazuo ; University of Kitakyushu, Dep. of Chemistry & Biochemistry

ARTICLE

Unraveling the kinetics of the structural development during polymerization-induced self-assembly: Decoupling the polymerization and the micelle structure†

Received 00th January 20xx,
Accepted 00th January 20xx

DOI: 10.1039/x0xx00000x

Rintaro Takahashi,‡[a] Shotaro Miwa,‡[a] Fabian H. Sobotta,[bc] Ji Ha Lee,[a] Shota Fujii,[a] Noboru Ohta,[d] Johannes C. Brendel,*[bc] Kazuo Sakurai*[a]

Upon extending a hydrophobic polymer chain from end of a preceding hydrophilic chain in aqueous solutions, the resultant block copolymers may eventually undergo self-assembly. Further chain propagation continues in the newly formed hydrophobic polymer rich domain. This process is often referred to as polymerization-induced self-assembly (PISA). Its kinetics are determined by the polymerization and the micelle formation/growth, which may influence each other, possibly leading to a highly complex process of structural development. In this study, we examined PISA in aqueous solution on the reversible addition fragmentation chain transfer (RAFT) dispersion polymerization of poly(*N*-acryloylmorpholine)-*b*-poly(*N*-acryloylthiomorpholine). Using *in situ* small-angle X-ray scattering (SAXS) and nuclear magnetic resonance spectroscopy (NMR), the polymerization and micelle formation were observed. In the analysis, because the time scale of the micelle formation/growth is much shorter than that of the polymerization, the polymerization and micelle fomarion/growth can be decupled. Thus, these were separately analyzed in depth, and a combination of the kinetics of RAFT polymerization and the simple scaling theory of the micellar structures can quantitatively describe the overall micellar structural development during PISA. The present study provides an unprecedented insight into the processes underlying PISA and deepens our quantitative understanding of it.

Introduction

Recent progress in controlled polymerization such as reversible addition-fragmentation chain transfer (RAFT) polymerization[1–3] and atom-transfer radical polymerization,[4,5] has provided a novel method to design new nano-materials. For example, one-pot preparation of micelles and vesicles becomes possible by use of the polymerization-induced self-assembly (PISA) *via* dispersion polymerization.[6–22] Fig. 1 illustrates PISA by use of sequential RAFT dispersion polymerization of two monomers A and B. Here, monomer A is polymerized with a RAFT agent in water, followed by the polymerization of monomer B started from the end of the polymer A to form a diblock copolymer (A-B). The monomer B can be dissolved in water, but the polymer B is water-insoluble. As the B-chain grows longer, A-B block copolymers may start segregating from water due to them becoming less water compatible. At a certain length of the B-chain, the A-B block copolymers form micelles. Considerable attention has been paid to PISA, since it enables to prepare micelles and vesicles with various intriguing morphologies and controlled size in a large scales and high concentrations.[6–22]

The present study concentrates on the kinetics of polymerization and micelle formation in PISA. This is an important aspect but has not received enough attention to comprehensively theoretically elucidate the entire process of micelle formation and polymerization. So far, Touve *et al.*[23] observed a PISA process in aqueous solutions of a block copolymer using liquid-cell transmission electron microscopy, while Derry *et al*.[24] and Alauhdin *et al*.[25] tracked a morphological change in PISA with a non-aqueous system (in mineral oil and CO2) by time-resolved small-angle X-ray scattering (SAXS). These works are *in situ* observation of PISA process combining morphological changes and polymerization kinetics, but it appears that the kinetics could not be completely understood particularly in terms of molecular mechanisms. In the work of Derry *et al*.,[24] they observed accelerated polymerization owing to extra radicals created by X-ray radiation and the kinetics under X-ray exposure was not the same as that without it. The same group studied PISA for poly(2-hydroxypropyl methacrylate) (PHPMA) as a core-forming block and found that the simple RAFT polymerization kinetics could not be used to describe the data because the local (or effective) monomer concentration changed during PISA.[8,26] Therefore, the quantitative detailed kinetics of

[a] *Department of Chemistry and Biochemistry, University of Kitakyushu, 1-1 Hibikino, Wakamatsu-ku, Kitakyushu, Fukuoka 808-0135, Japan*
[b] *Laboratory of Organic and Macromolecular Chemistry (IOMC), Friedrich Schiller University Jena, Humboldtstrasse 10, 07743 Jena, Germany*
[c] *Jena Center for Soft Matter (JCSM), Friedrich Schiller University Jena, Philosophenweg 7, 07743 Jena, Germany*
[d] *Japan Synchrotron Radiation Research Institute (JASRI/SPring-8), 1-1-1 Kouto, Sayo, Sayo, Hyogo 679-5198, Japan*
† Electric supplementary information (ESI) available. See DOI: 10.1039/x0xx00000x
‡ These authors contributed equally to this work.

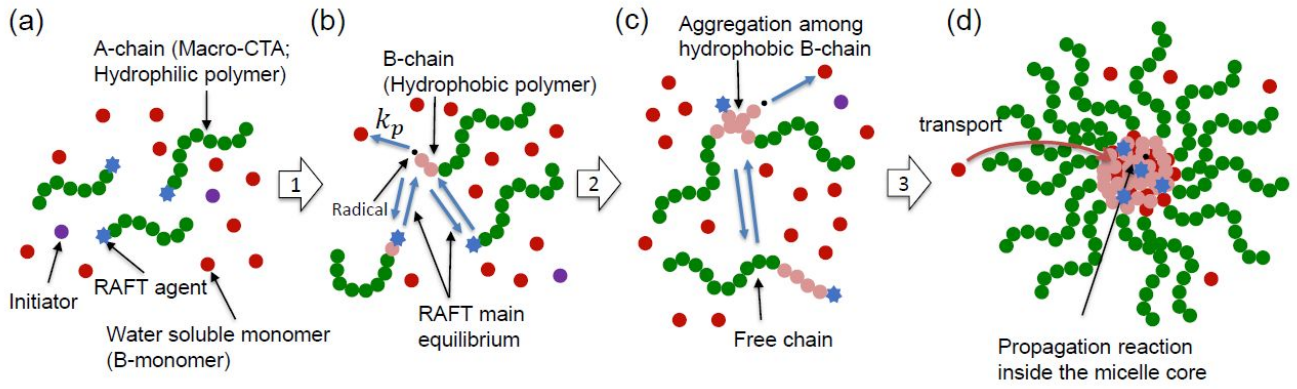

Fig. 1 A schematic illustration of a PISA process *via* the second RAFT dispersion polymerization of monomer B to form a spherical micelle in water from A-B diblock copolymers. (a) Monomer B and initiator is added to a macro-CTA consisting of hydrophilic A-chain and RAFT agent. (b) Main equilibrium between dormant species and active polymer chains. The radical at the end of the active polymer reacts with monomer B and subsequent chain propagation occurs with the rate constant of k_p. (c) Polymerization of the monomer B propagates and eventually the hydrophobic B-chains start to aggregate, coexisting in an equilibrium with free chains. (d) Micelles with the core−shell structure are formed, and the RAFT polymerization events (chain propagation, initiator formation, and termination) now occur inside of the micellar core in which the monomer B concentration may be different from the macroscopic (or overall) monomer B concentration.

micelle formation in PISA has remained unclear, particularly with regard to the quantitative molecular mechanisms involved.

A potential reason for this lack of progress is that the kinetics of the polymerization itself is complicated in PISA as follows. When the polymerization the polymerization of solvophobic block B proceeds, micellar formation takes place at certain points, and the micellar formation and polymerization may interfere with each other. Understanding such concurrently occurring events appears to be difficult. Examples of this include the following: (i) The composition of A and B within the block copolymer changes and thus the solvent compatibility may differ between the early and late stages of polymerization (see b-d in Fig. 1), which may affect the polymerization kinetics. (ii) In particular, after micellar formation, most of the macro-chain transfer agents (macro-CTA) are concentrated inside the core[27] and thus their overall concentration [$C_{I2}(0)$] is not equal to the effective local concentration of macro-CTA in the core. This may drastically affect the reaction rate, which may have occurred in the work of Warren *et al.*[8,26] Another issue is that (iii) the propagation reaction of the B chain may be affected by the formation of micelles (illustrated in Fig. 1) because monomer B has to enter the micelles to be involved in polymerization after micellar formation, or monomer B may be concentrated in the B-chain core because it may has a greater affinity for the B-core than for the solvent, as mentioned by Warren *et al.*[8,26] The overcrowding shell chains and solid-like core may slow down the diffusion of monomer B. These issues are similar as in the case of non-controlled emulsion polymerization.[28,29]

Besides the complexity in the kinetics of polymerization in PISA, the micelle formation/growth and polymerization simultaneously take place. Therefore, the kinetics of this process is fascinating but also complicated. We suppose that no kinetic model thus has been established to describe PISA and its molecular mechanism has not been analysed in depth.

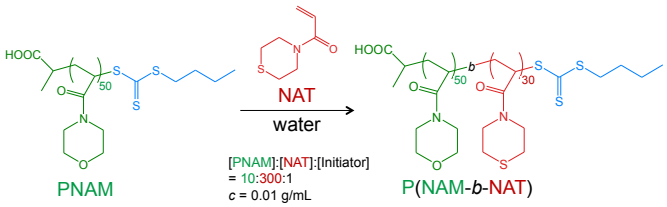

Fig. 2 Chemical Reaction to Form P(NAM-*b*-NAT): Block copolymer composed of *N*-acryloylmorpholine (NAM) and *N*-acryloylthiomorpholine (NAT) from the end of the preceding PNAM chain, where NAM and NAT are the monomers A and B in Fig. 1, respectively.

In this study, we investigate the kinetics of PISA (structural development during PISA) in a block copolymer composed of *N*-acryloylmorpholine (NAM) and *N*-acryloylthiomorpholine (NAT) denoted as P(NAM-*b*-NAT) in aqueous solution (*cf*. Fig. 2). It was reported that PNAM can be polymerized in water by RAFT achieving full conversion (> 99%) while the high livingness is maintained.[30,31] Moreover, it was recently demonstrated that PISA *via* RAFT dispersion polymerization with full conversion works well for the formation of spherical micelles of P(NAM-*b*-NAT) in an aqueous system.[32] PNAM is a hydrophilic polymer or macromolecular chain-transfer agent (macro-CTA), respectively. Spherical micelles are formed with the subsequent polymerization of NAT, and this micellar structure was characterized by dynamic light scattering, nuclear magnetic resonance spectroscopy (NMR), size-exclusion chromatography (SEC), and cryogenic transmission electron microscopy in a previous work.[32] For this system, in the present work, NMR and *in situ* time-resolved SAXS measurements at SPring-8[33,34] has been performed to monitor the kinetic process of PISA, and the obtained data have been intensively analysed by a newly proposed way to comprehensively characterize PISA.

Experimental

Materials

NAT and PNAM (macro-CTA) were prepared in the same manner as described previously.[32] The number-average molecular weight ($M_{n,PNAM}$) and degree of polymerization of PNAM ($n_{n,PNAM}$) were determined to be 7100 and 50, respectively, by ^{1}H NMR spectroscopy. The dispersity index of PNAM was 1.1, as determined by SEC. An initiator {2,2'-azobis[2-(2-imidazolin-2-yl)propane] dihydrochloride; VA-044} was purchased from Fujifilm Wako Pure Chemical and used without any purifications. Water was purified using a Milli-Q system (Merck Millipore).

Preparation of the solutions

PNAM, NAT, and the initiator were dissolved in pure water. The molar ratio of PNAM:NAT:initiator was 10:300:1. As such, the degree of polymerization of NAT ($n_{n,PNAT}$) was expected to eventually reach around 30, in the case of full conversion. This solution was degassed by purging with nitrogen gas for ca. 30 min before the performance of PISA. The total solute concentration (c) was 0.01 g/mL. This concentration was dilute enough to ignore the inter-particle scattering, otherwise the SAXS analysis would have been difficult. We note that this concentration is relatively dilute; thus, the reaction rate of polymerization was smaller than that of the previous studies on PISA.[6–22] However, as discussed later, the observed micellar structure was considered same as those in the higher concentrations.

Time-resolved SAXS

The *in situ* synchrotron time-resolved SAXS measurements were conducted at the BL40B2 beamline, SPring-8, Sayo, Japan. The sample solution was filled into a capillary cell with a diameter of 2 mm (Hilgenberg GmbH, Malsfeld, Germany), which was sealed using an epoxy resin (Araldite; Huntsman, The Woodlands, TX), under a nitrogen atmosphere in a glove box. The capillary cell was attached to an aluminum holder, and the holder with the cell was then put on a thermostat (HCS302; Instec, Inc., Boulder, CO), for which the temperature (T) was set to 70, 80, or 90 °C to trigger the polymerization. We confirmed that the solution temperature reached the target one within *ca*. 30 s. Immediately after the cell had been put on the thermostat, we started to measure the time (t). We performed repeated sessions of X-ray exposure for 2 min. The scattering intensity was recorded using a PILATUS 2M detector (Dectris, Baden, Switzerland) in which the camera length was 4 m. After 75, 40, and 24 min for 70, 80, or 90 °C, respectively, no appreciable changes in the scattering were observed; thus, the data acquisition was terminated.

With azimuthal averaging, the obtained 2D images were converted to be 1D scattering profiles of the scattering intensity vs. the magnitude of the scattering vector (q). Here, q is defined by $q \equiv (4\pi/\lambda)\sin(\vartheta/2)$ with the wavelength of the incident X-ray (λ = 0.1 nm) and the scattering angle (ϑ). The q range of 0.03−1.9 nm^{-1} was accessible in the setup of this study. The scattering from the background was subtracted, and the obtained excess scattering intensity was transformed into the differential scattering cross-section per unit volume [$I(q)$] by using water as a standard material.[35] In the analysis of the SAXS profile, the $I(q)$ value was divided by the constant (K_e) and c. Here, K_e is defined by $K_e \equiv N_{Av}r_e^2\gamma_{ave}^2$ with the average contrast factor (γ_{ave}; *cf.* the Supporting Information of Ref. 36), Avogadro's constant (N_{Av}), and the classical electron radius (r_e). The densitometry (a density/specific gravity meter DA505; Kyoto electronics manufacturing) was performed to estimate the density or partial specific volume for the analysis of the SAXS data.

It is always possible that synchrotron X-rays may interfere with samples and experiments. In the worst case, this leads to the decomposition of samples, referred to as radiation damage. It is well known that high-energy light causes the cleavage of chemical bonds to create radicals. Even if there is no radiation damage in samples, the radicals created by the X-rays may accelerate polymerization.[37,38] Here, the effects of radiation were carefully examined at 25 °C, at which no RAFT polymerization occurs owing to the limited decomposition of the initiator. As a control experiment, we performed X-ray exposures in the same manner as in the experiments described above except for the applied temperatures, and compared the scattering profiles for the first and final frames so as to determine whether there was any appreciable change. We found that an attenuator (an aluminum sheet with a thickness of 12 μm) is needed to reduce the X-ray intensity (ca. 7 × 10^9 photons/s), and the c value had to be low values of 0.01 g/mL. In time-resolved SAXS measurements, it is generally better to set a short acquisition (or X-ray exposure) time and a long interval between the acquisitions. The application of stronger X-ray enables in shortening the acquisition time, but is associated with beam damage problems as mentioned above. We selected this beamline and used an attenuator to make the incident X-ray intensity weaker. Because of this weak X-ray intensity, we needed to set an acquisition time of 2 min and the shortest interval time of 2 s. The sampling time (t) was set to the centre of the acquisition duration (*ie*., 1 min after acquisition started). We are aware that the obtained scattering is considered to be time-averaged over 2 min and there may thus be some ambiguity in the measurements especially in earlier stage.

NMR spectroscopy

The *ex situ* ^{1}H NMR spectroscopy was performed using a JNM-ECP500 NMR spectrometer (JEOL Ltd., Tokyo, Japan) with a frequency of 500 MHz, similarly to the process used in a previous study.[32] The polymerization was run in a vial with a diameter of 7 mm at T = 70, 80, and 90 °C. For the solvent, deuterated water was used. Each solution volume was *ca.* 0.5 mL, and a thermometer was used to check that the solution temperature reached the target temperature within 30 s. Some of the solutions was taken up in each of the intervals between the polymerization. Each obtained solution was diluted with deuterated water to c = 0.001 g/mL to run the *ex situ* NMR measurements. The conversion of NAT [$p(t)$] was determined by the ratio of the vinyl proton signals (NAT) to the terminal methyl proton signals (CTA) (*cf.* Fig. S3).

Results

Time-resolved SAXS measurements during NAT polymerization

Fig. 3 shows the time evolution of the SAXS profiles upon the RAFT polymerization of NAT at T = 70, 80, and 90 °C, compared with the initial state (T = 25 °C) indicated by grey circles. For clarity in viewing and simplicity, a typical scattering profile for each stage is shown in the figure. The profile for the initial state can be fitted by a Gaussian chain model with a radius of gyration of 2.0 nm. After heating the solution, which initiates the polymerization of NAT, it is apparent that the scattering profiles showed dramatic changes as follows:

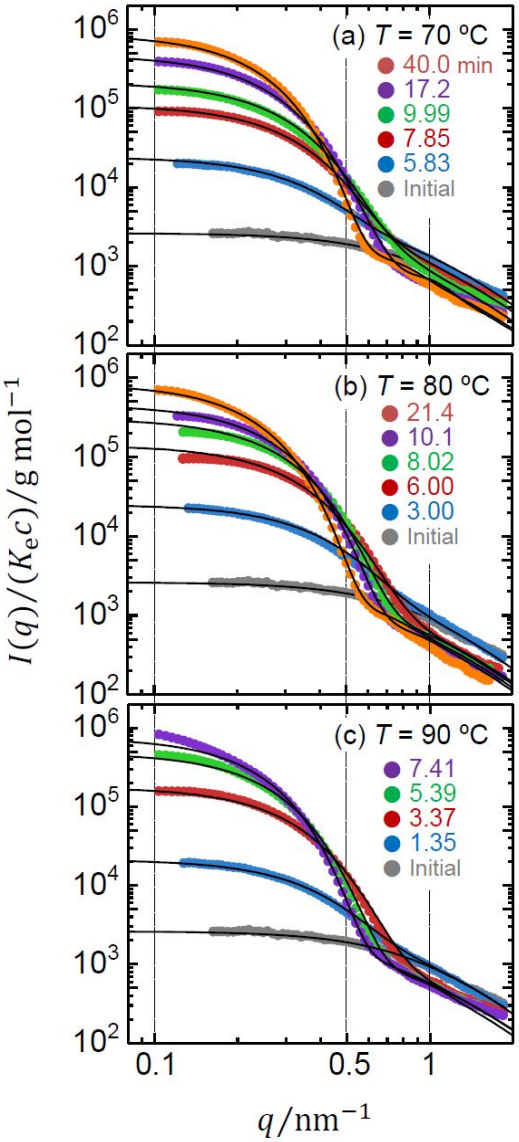

Fig. 3 Time evolution of the SAXS profiles during PISA at 70 °C (a), 80 °C (b), and 90 °C (c). For the visibility, 5 out of 20, 5 out of 15, and 4 out of 11 profiles are shown for 70, 80, and 90 °C, respectively. Black solid curves represent the curves fitted by the model scattering function (eqs 2–4). The gray data points represent the SAXS profiles at 25 °C corresponding to the initial state and were fitted by a Gaussian chain model with a radius of gyration of 2 nm and a cross-sectional diameter of 0.5 nm (*cf.* Fig. S5 and Table S2). See also Fig. S4 where the data are shown as the Kratky plots.

(i) The exponent (α) in the case of expressing $I(q) \propto q^{-\alpha}$ appeared to converge as $\alpha \rightarrow 0$ in the limit of the small-q, such as $q <$ 0.1 nm^{-1}. This indicates that the present q range, *ie.*, the camera length, is adequate to cover the size of the scattering objects for all stages. (ii) The forward scattering intensity in this small-q range increased by about two to three orders of magnitude in the later stage of polymerization. This increased forward scattering intensity suggested an increased the weight-average molar mass of the solutes[39] upon polymerization. The intensity would have been increased by about two and a half times if the increased weight-average molar mass of all the solutes had been ascribed simply to chain elongation of the NAT block. The $I(q)$ values at the small-q region increases in a few orders of magnitude, indicating the occurrence of aggregation from several block copolymers. The rather steep angular dependence in $I(q)$ at the intermediate q range suggested the formation of a scattering object with a narrow dispersity in size and shape, which is most likely to be micelles. (iii) $I(q)$ at the intermediate region (q = 0.3–0.6 nm^{-1}) showed a steep decrease with increasing q and this tendency became significant as the polymerization proceeded; α reaches a higher value at the later stage. This feature indicates the spherical morphology. The change in the angular dependence of $I(q)$ at the intermediate region during PISA is also clearly seen in the Kratky plots [$q^2I(q)$ vs. q; Fig. S4]. (iv) The exponent α became ~ 2 at the large-q region, such as 1.0 nm$^{-1} <$ q. The slope can be ascribed to scattering from flexible chains, and thus may be related to scattering from the micelle-bounded or/and free chains.

All of these features indicate that the spherical micelles are formed over time. Comparing the three temperatures, the higher temperature showed more rapid change. This indicates that the elevated temperature accelerated the RAFT polymerization, as it is well known.[1–3] All of the present findings reveal success in tracking the PISA process occurring during the polymerization of NAT.

NMR measurements during the polymerization and monomer conversion

Fig. 4 plots $p(t)$ against t for the three temperatures. As expected, the reaction was accelerated by increasing temperature, which is reasonable as the initiator decomposition and the propagation reaction are known to become faster.[30,31] The temperature dependence observed in the NMR results qualitatively agrees with the SAXS results. From the results of SEC at each time point, the

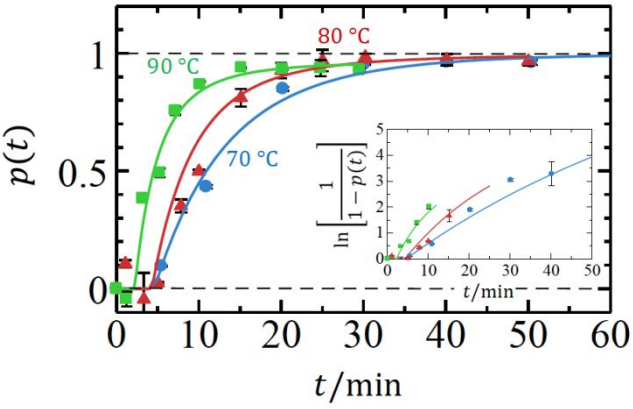

Fig. 4 Time-evolution of the conversion [$p(t)$] obtained by ^{1}H NMR for PISA at 70 °C (blue circles), 80 °C (red circles), and 90 °C (green circles). The solid curves are calculated by eq 1 with the parameters listed in Table 1. Inset: The plots of ln{[1 − $p(t)$]$^{-1}$} against t for the same data at the early

dispersity indices of less than 1.15, and the molecular weight distribution remained unimodal (Figs. S1 and S2). The theoretical number fractions of living chain were calculated by eq S12[40] to be 0.93 (at 70 °C; 50 min), 0.92 (at 80 °C; 30 min), and 0.91 (at 90 °C; 20 min). Hence, the RAFT polymerization proceeded well up to the full conversion and with good control under these conditions.

Discussion

Polymerization kinetics of NAT

RAFT polymerization consists of initiation (decomposition of initiator), addition of radical species to CTA, equilibrium between active and dormant species with the growth of polymer chains, and termination. It is known that kinetics of RAFT polymerization is similar to those of conventional radical polymerization.[1,2] Thus, we can calculate the time dependence of the monomer (NAT) concentration [$C_{NAT}(t)$] by the model for the kinetics of conventional radical polymerization:[2]

$$\frac{C_{NAT}(t)}{C_{NAT}(0)} = \exp\left\{2k_p\sqrt{\frac{fC_{I_2}(0)}{k_d k_t}}\left[\sqrt{\exp(-k_d t)}-1\right]\right\} \quad (1)$$

where k_d and k_t denote the reaction rate constants in the decomposition of the initiator and the termination, respectively. In this calculation, we assume that polymerization of NAT would start from the end of PNAM without any side reactions. Although eq 1 is for conventional radical polymerization, It is known to be applicable for RAFT polymerization.[2] eq 1 is derived under the assumption that the rate constant of the chain propagation (k_p) does not depend on the chain length of PNAT, and the radical concentration is constant. The detailed derivation is given in ESI. There is however an induction time (t_{ind}) caused by the retardation of RAFT polymerization,[1] and thus t in eq 1 should be replaced by $t - t_{ind}$, and we set $C_{NAT}(t) = 0$ for $t < t_{ind}$. f is the efficiency of the initiator and $f = 0.5$ was used in this study as it has been known for similar azo-type initiators.[2] p(t) can be calculated from the relation of $p(t) = [C_{NAT}(0) - C_{NAT}(t)]/C_{NAT}(0)$.

The major factor determining the temperature dependence of the RAFT polymerization rate is the decomposition of the initiator. It is known that the k_d value for the azo-initiator used in the present system has an Arrhenius-type activation energy of 108 kJ mol^{-1} and $k_d = 1.16 \times 10^{-3}$ min^{-1} at 44 °C.[30] The k_d values at 70, 80, and 90 °C were determined by these two relations. We fitted eq 1 to the experimentally-obtained data with the adjustable parameters of $k_p/\sqrt{k_t}$ and t_{ind}. k_p also depended on the temperature but was less sensitive than k_d in the present case. The fitted curves are presented by solid curves in Fig. 4, and the parameters used in the fitting are listed in Table 1.

As shown in Fig. 4, the agreement between the calculation and the experimental data is reasonably good, especially for 90 °C. This means that $k_p/\sqrt{k_t}$ did not seemingly change until the conversion reached almost 100% despite the aggregation of the PNAT blocks. This result is in contrast to the report by Warren *et al.*[26] They observed that the RAFT polymerization of poly(2-hydroxypropyl methacrylate) (PHPMA) was dramatically accelerated in the middle of the reaction when the micellar formation occurs, because the HPMA monomer became solubilized in the micellar core and thus the effective HPMA concentration was increased (*ie*., the overall monomer concentration is not the same as the effective one).[26] In addition, the increase in the effective concentration should leads to the decrease in k_t. This point is discussed later.

Table 1 Parameters (rate constants and induction time in the RAFT polymerization) in the fitting of the conversion data (Fig. 4) by eq 1

T / °C	k_d / 10^{-2} min^{-1} [a]	$k_p k_t^{-1/2}$ / (mol^{-1} L min^{-1})$^{1/2}$	t_{ind} / min
70	2.57	57 ± 2	4.6 ± 0.2
80	7.51	57 ± 2	4.2 ± 0.2
90	20.7	59 ± 2	2.2 ± 0.2

[a] k_d at each temperature was calculated from the Arrhenius-type activation energy of 108 kJ mol^{-1} and $k^d = 1.16 \times 10^{-3}$ min^{-1} at 44 °C.[30]

Analysis of the SAXS profiles to evaluate the structural parameters

The SAXS profiles in Fig. 3 suggest the formation of micelles upon polymerization of NAT. Therefore, in the analysis, we assumed that unreacted monomers (NAT) and micelles coexist with a weight fraction of NAT [$w_{NAT}(t)$]. In such a case, $I(q,t)$ is given by[41]

$$\frac{I(q,t)}{K_c c} = \frac{1}{\gamma_{ave}^2}\left\{\gamma_{NAT}^2 w_{NAT}(t) M_{NAT} + \gamma_{poly}^2(t)[1-w_{NAT}(t)]M_{w,mic}(t)P_{mic}(q,t)\right\} \quad (2)$$

Here, we explicitly show the time-dependent quantities as $X(t)$. γ_{NAT} and $\gamma_{poly}(t)$ stand for the contrast factors of NAT and the polymer, respectively (*cf*. ESI and Ref. 36). M_{NAT} is the molecular weight of the unreacted monomer of NAT, whilst $M_{w,mic}(t)$ is the weight-average molar mass of the micelle. $P_{mic}(q,t)$ is the form factors of the micelle and we used the core–corona spherical micelle model,[42] since it is known that P(NAT-*b*-NAM) forms a spherical micelle at $n_{n,PNAM} = 50$ and $n_{n,PNAT} = 30$,[32] and the shape of the SAXS profiles indicated the spherical morphology as mentioned above. Regarding the scattering from the unreacted NAT, the size is sufficiently small not to show any angular dependence of the scattering in the present q range. In eq 2, $w_{NAT}(t)$, $M_{w,mic}(t)$, and $P_{mic}(q,t)$ depend on time. Among them, $w_{NAT}(t)$ is calculated from $p(t)$ through eq S11 and $M_{w,mic}$ can be determined with extrapolating $I(q)$ to $q = 0$. All of the angular dependence of the scattering profiles is ascribed to $P_{mic}(q,t)$ given by:[42]

$$P_{mic}(q,t) = \left\{f_C(t)E_C(q,t) + [1-f_C(t)]E_S(q,t)\right\}^2 + \frac{[1-f_C(t)]^2}{N_{agg}(t)}[E_S^2(q,t) - E_{ch}^2(q)] \quad (3)$$

Here, N_{agg} is the aggregation number, f_C is the contrast of the core domain within the micelle (*cf.* eq S14). $E_C(q,t)$ and $E_S(q,t)$ are the scattering amplitudes from the core and shell, respectively, expressed by:

$$E_C(q,t) = \frac{3\{\sin[qR_C(t)] - qR_C(t)\cos[qR_C(t)]\}}{[qR_C(t)]^3}\exp(-\sigma q) \quad (4)$$

$$E_S(q,t) = \frac{1-\exp\left(-q^2R_{g,S}^2\right)}{q^2R_{g,S}^2}\frac{\sin\left\{q\left[R_C(t)+R_{g,S}\right]\right\}}{q\left[R_C(t)+R_{g,S}\right]}\exp\left(-\sigma q\right) \quad (5)$$

$E_{ch}(q)$ in eq 3 is the scattering amplitude from the individual shell chain, given by eq S14. $R_C(t)$ is the radius of the micellar core, $R_{g,S}$ is the radius of gyration of the shell chain, and σ is the thickness of the core−corona interface. These parameters can be evaluated from fitting (see ESI for details). The best-fitted curves are shown in Fig. 3 as black solid curves. Except for the low-q data at 7.41 min at 90 °C, the agreement between the experimentally-obtained data and calculation was good, and $M_{w,mic}(t)$ and R_C(t) were uniquely determined at each time by the fitting. Sometimes, as in the profile of 7.41 min at 90 °C, we observed the up-ward deviation, and this can be ascribed to a small amount of secondary aggregates. For such a case, we obtained the value of $\lim_{q\to 0}[I(q)/(K_ec)]$ by use of the Guinier plot[39] (the scattering from the secondary aggregates was ignored). The N_{agg} and R_C values obtained by this manner are plotted against t in Fig. 5.

The number-average molecular weight of PNAT block [$M_{n,PNAT}$(t)] can be calculated from $p(t)$ and k_d as a function of time:[2]

$$M_{n,PNAT}(t) = \frac{C_{NAT}(0)M_{NAT}}{C_{PNAM} + 2fC_{I_2}(0)[1-\exp(-k_dt)]}p(t) \quad (6)$$

where C_{PNAM} is the molar concentration of PNAM. We assumed that the radical-radical termination event occurs only through bimolecular termination by disproportionation. The number-average molecular weight of the block copolymer of P(NAM-*b*-NAT) [$M_{n,PNAM\text{-}b\text{-}PNAT}(t)$] is obtained by $M_{n,PNAT}(t)$ + $M_{n,PNAM}$ with the $M_{n,PNAM}$ value of 7100. N_{agg} is now calculated from $N_{agg}(t) = M_{w,mic}(t)/M_{n,PNAM\text{-}b\text{-}PNAT}(t)$. All of the numerical data are summarized in ESI. We note that $M_{n,PNAT}(t)$ was evaluated to be zero at the first frame in the time-resolved SAXS data (3.00 min at 80 °C, and 1.35 min at 90 °C), although the scattering profiles showed the formation of aggregates. We decided to omit the first frame in the time-resolved SAXS data in the following discussion and we suppose that this error may be ascribed to the long acquisition time. Fig. 5 shows that immediately after polymerization started, N_{agg} drastically increased. This result indicates that once even a small portion of hydrophobic PNAT attaches to the hydrophilic PNAM, the entire block copolymers become insoluble in water to induce aggregation.

Dependence of N_{agg} and R_C on the chain length of the PNAT core

In Fig. 6, N_{agg} and R_C are double-logarithmically plotted against $M_{n,PNAT}$. All data points for different temperatures can be fitted by one straight line. Thus, when we express $N_{agg} = aM_{n,PNAT}^{\beta}$ and $R_C = bM_{n,PNAT}^{\gamma}$, it is possible to use the same a, β, b and γ values for different temperatures. This is an important result because it suggests that (i) a single physical principle governs the micellar formation over the entire time range and temperature, (ii) the chain

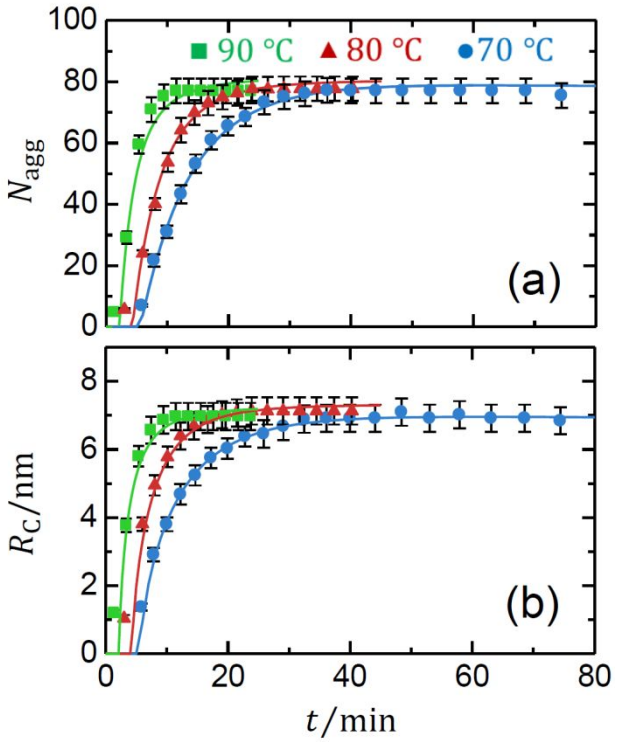

Fig. 5 Aggregation number (N_{agg}; a) and radius of the micellar core (R_C; b) as functions of time. The blue circles, red triangles, and green squares represent the data obtained by *in situ* time-resolved SAXS at 70, 80, and 90 °C, respectively. The solid curves represent the curves fitted by the model of the kinetics described later.

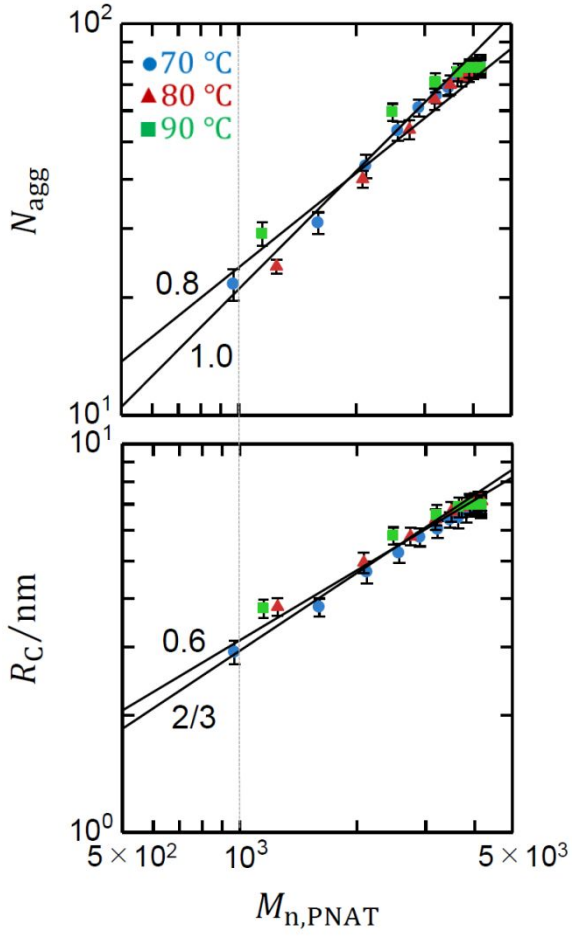

Fig. 6 N_{agg} and R_C as functions of the molecular weight of the core-forming block ($M_{n,PNAT}$) during the PISA process. The blue circles, red triangles, and green squares represent the data obtained at 70, 80, and 90 °C, respectively.

length, namely $M_{n,PNAT}$, is the only parameter to determine the structures, and (iii) temperature dependence of the micellar structures is negligibly small. *ie*., once $M_{n,PNAT}$ is given, the micellar structures are determined. It is surprising that, despite a difference of one order of magnitude in the polymerization rate (between 70 and 90 °C), the same structures arose. The scaling exponents of β and γ were evaluated to be $\beta = 0.95 \pm 0.05$ and $\gamma = 0.64 \pm 0.03$. The core size is related to N_{agg} through $R_C \propto (N_{agg}M_C)^{1/3}$ because of the simple mass balance, where M_C is the molecular weight (or chain length) of the core-forming block chain. Therefore, $\gamma = (1 + \beta)/3$ because of $N_{agg} \propto M_C^{\beta}$. The obtained β and γ values well satisfy this relation.

A simple scaling model of block copolymer micelles was proposed by de Gennes,[43] under the assumption that the core-forming block chains are completely segregated from both the shell chains and the solvent molecules, forming a melted core. The shell chains and solvent molecules are uniformly mixed in the shell region, and the core chains are uniformly stretched with the end-to-end distance and equal to R_C. In this model, the elastic deformation, namely, conformational entropy of the core chain plays an important role determining N_{agg} and the model predicts that β = 1.0. By analogy with the overlap concentration (c^*), which is the boundary between the dilute and semidilute regimes of polymer solutions, the crowding of the shell chains can be classified into two regions: (a) isolated and (b) overcrowded as illustrated in Fig. 7. Here, the touching state corresponds to c^*. The de Gennes model is only good for (a) and (b) states. Zhulina and Birshtein,[44] and Halperin[45] used the star polymer model formulated by Daoud and Cotton[46] to describe the shell chains for case (c). The shell chains are partially stretched in the radial direction due to the crowded chains in the core–shell interface, while this chain orientation becomes close to a random conformation at the water–shell interface. This means that the spatial size in which a polymer chain can behave as a random coil, denoted by the blob size (ξ_b), is small at the core–shell interface and increases when approaching the

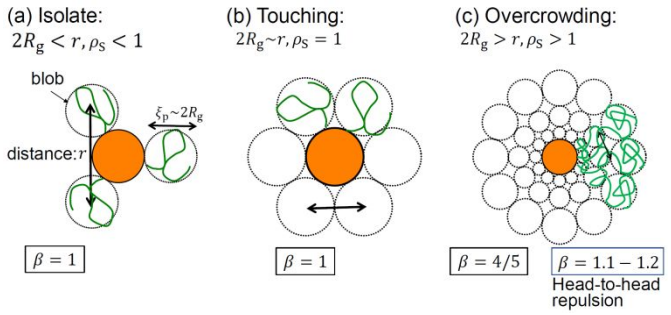

Fig. 7 Two representative crowding states of the shell chains tethered on the spherical core; (a) the shell chains are well-isolated and thus the shortest distance between the two chains (r) is larger than twice the radius of gyration (R_g) and the blob size (ξ_b) is close to R_g. (b) This shows the cross-over state between (a) and (c). In the state of (c), the shell chains are overcrowded and $2R_g > r$ and the blob size is proportional to the distance from the core center. ρ_S is an indicator of the crowding of the shell chains defined by eq 7.

water-shell interface. According to these two theories, β is predicted to be 4/5. However, they do not take into account the repulsive interaction between the hydrophilic head groups. Nagarajan and Ganesh[47–50] introduced the osmotic and elastic contribution into the Daoud and Cotton model[46] and found β = 1.1 – 1.2 for a good solvent of the shell chains in case (c). Their model well explained the various experimentally-obtained data such as poly(propylene oxide)-*b*-poly(ethylene oxide) and polystyrene-*b*-polybutadiene systems. This suggests that the shell block gives stronger dependence of N_{agg} than the previous models, and thus, the repulsions (or osmotic contribution) of the shell chains are important for block copolymers. Nagarajan and Ganesh[48–51] also formulated a relationship when the core is swollen by solvent, and the solvent/core-chain interaction has molecular weight dependence through the Flory χ parameter. The above-mentioned models and predictions of the scaling exponents of β are summarized in Fig. 7.

Fig. 6 only covers one order of magnitude of the molecular weight and shows some experimental error in the slope. Therefore, it may be difficult to evaluate an exact value of β and which model is more appropriate to analyse the data, but it is certain that $\beta \leq 1$. This means that the head-to-head repulsion may not be present in our system and the shell chains may not exhibit much overcrowding.

Nature of the Core and Shell Chains

The level of crowding of the shell chains is an essential issue to discuss the M_C dependence of N_{agg}. We estimated the density of the shell chain (ρ_S) according to the equation by Svaneborg *et al*.:[51]

$$\rho_S = \frac{\pi R_{g,S}^2 N_{agg}}{4\pi (R_C + R_{g,S})^2} \quad (7)$$

We used $R_{g,S}$ = 2.0 nm at 70 and 80 °C and 1.9 nm at 90 °C determined from SAXS (*cf.* ESI). The denominator is the surface area of a sphere with a radius of $R_C + R_{g,S}$ (definition), and the numerator is the sum of the cross-sectional area of the shell chains (*ie*., The surface area occupied by the shell chains). Hence, $\rho_S > 1$ reflects an overcrowded state, while $\rho_S < 1$ indicates an isolated one. All of the parameters in eq 7 are already known; thus, we calculated ρ_S at each time point, as shown in Fig. 8a. In the early stage, ρ_S rapidly increased and later converged to about 1 at all the temperatures, indicating that the PNAM chains are in an isolated or touching state. The convergence value differed slightly for each temperature. At 70 °C, ρ_S reached almost 1.0, but at 90 °C, it was about 0.9. The important fact here is that the shell chains are not so overcrowded and the de Gennes model[43] may be appropriate.

The segment mass concentration in the core ($c_{w,NAT}$) can be calculated by:

$$c_{w,NAT} = \frac{N_{agg}\left(\frac{M_{n,PNAT}}{N_{Av}}\right)}{\frac{4}{3}\pi R_C^3} \quad (8)$$

Fig. 8b shows the development of $c_{w,NAT}$ over time for each temperature. Similar to panel a, $c_{w,NAT}$ rapidly increased in the early stage and reached a different value for each temperature. A higher temperature gave a lower $c_{w,NAT}$ and all values of $c_{w,NAT}$ were much

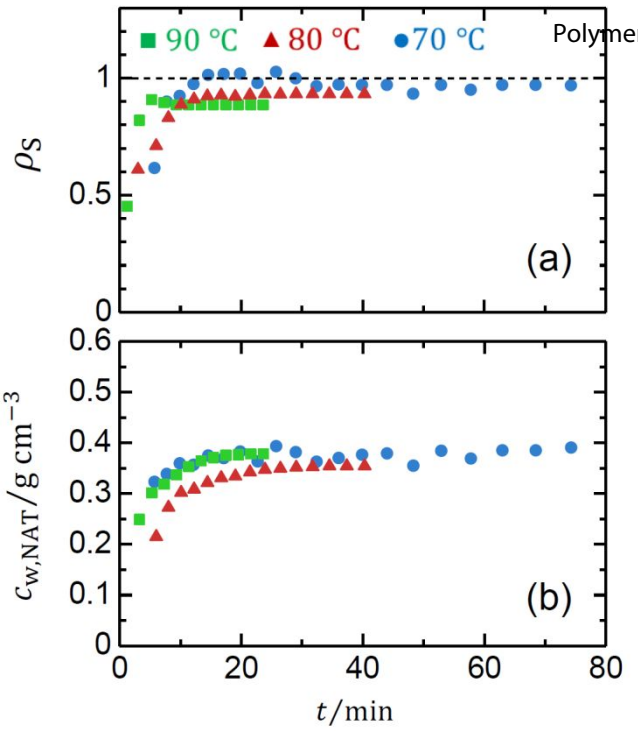

Fig. 8 The density of the shell chain (ρ_S) in the panel a and the segment concentration in the core ($c_{w,NAT}$) in the panel b as functions of time. See also Fig. S6 where ρ_S and $c_{w,NAT}$ are plotted against $M_{n,PNAT}$.

lower than 1. The mass density of PNAT in water determined by densitometry is about 1.2 g/cm^3. The observed values of $c_{w,NAT}$ = 0.4 g/cm^3 are much smaller than it. This means that a substantial amount of water is contained in the core. In fact, this concentration of 0.4 g/cm^3 is normally observed for the polymer-rich phase of a phase-separated solution in homopolymer/poor solvent systems.[52] Furthermore, $c_{w,NAT}$ = 0.4 g/cm^3 is smaller than the overlap concentration (c_{NAT}^*) calculated by $c_{NAT}^* = M_{n,PNAT}/[(4/3)\pi N_{Av} R_{g,PNAT}^3]$ with the radius of gyration of PNAT chain ($R_{g,PNAT}$), calculated assuming the coil limit[53] with the contour length per the repeating unit of 0.25 nm.

The $M_{n,PNAT}$ dependence of N_{agg} (Fig. 6) indicates that β = 1.0 and the de Gennes model[43] is appropriate for our system. The discussion of ρ_S also supports the de Gennes model, while that of $c_{w,NAT}$ is contrary to the preconditions of the model; the core is excluded from the solvent molecules. According to his scaling theory, the standard chemical potential of the micellar formation per chain ($\Delta\mu_0$) is given by:

$$\Delta\mu_0 \propto \frac{R_C^2}{M_C} + \eta\frac{M_C}{R_C} \quad (9)$$

Here, η represents the interfacial tension parameter, the first term describes the stretching free energy of the chains in the core region, and the second term is the free energy of the formation of the interface between the core and shell. The first term is derived from the relation that the conformational entropy of a Gaussian chain with an extended end-to-end distance (R_e) is given by $R_e^2(3k_BT)/(2na_S^2)$ with k_B, n, and a_S being the Boltzmann constant, the number of segments, and the segment length.[54] Note that n is proportional to M_C, and na_S^2 is equal to the square of the end-to-end distance of the Gaussian chain with no extension. In the original model of de Gennes,[43] he treated the core as being in a melted state. However, eq 9 may be used for the solvent-swollen core by the same n and a_S in the case of $c_{w,NAT} < c_{NAT}^*$, and Gennes model fits to the experimentally-obtained data.

The Polymer Concentration Dependence of the Spherical Micellar Structures

The segment concentration within the micelle core is expected not to depend on the concentration of the solution for the following reason. Sato *et al.*[55] discussed the micellar formation from A-B block copolymers in water on the analogy of the phase diagram for B-homopolymer/water systems,[52] where A is always water-soluble and B change from water-soluble to -insoluble, assuming the micelle formation is considered as a phase-separation. The micellar core can be regarded as a B-block rich phase and the B-block concentration in this phase does not depend on the overall polymer concentration, but the volume fraction is changed in accordance with the lever rule. The micellar size is determined by balance of the free energy of the core and shell domains, similar to eq 9. Therefore, if the concentration within the core is fixed, the micellar size would not change, while the number of micelles in the solution changes, by increasing the concentration of the solution. To confirm this expectation, we performed *ex situ* SAXS measurements for P(NAT-*b*-NAM) micelles at c = 0.055 g/mL after the full-conversion at 70 °C in PISA, as shown in Fig. S7. The analysis of the SAXS profile indicates that the spherical micelles are formed, and the concentration within the core is 0.4±0.01 g/cm^3, which is the same as in the case of c = 0.01 g/mL.

In the *in situ* time-resolved SAXS, the concentration (c = 0.01 g/mL) of the solution is lower than that in previous reports on PISA for spherical micelle formation (typically 0.05–0.1 g/mL).[8,32] However, on the basis of the above result and discussion, $c_{w,NAT}$ is considered to be almost independent of c, and thus, the structural development in the present concentration is not atypical, and our proposed analytical way may be applied to any PISA cases to form spherical micelles.

Hypothesis for Decoupling the Kinetics of the Polymerization and the Micelle Structure in PISA.

In the present RAFT polymerization, approximately 50 min was required for complete conversion of the monomer at 70 °C, while the micellar formation of P(NAM-*b*-NAT) appeared to be much faster than the polymerization, although we did not measure its accurate time scale. According to the papers regarding the kinetics of micellar formation and growth (*via* unimer exchange or fusion/fission) in block copolymers,[56–67] the times to reach the equilibrium in micelle formation and growth are typically within 1 s (as summarized in Table S1). It is therefore reasonable that our micellar formation occurs on a similar time scale. In consequence, the polymerization is sufficiently slower than the micelle formation/growth, in other words, the rate-determining process of the structural development in PISA is the polymerization. Therefore, we only need to consider the polymerization process when focusing on the kinetics. After that, the micelle structure can be independently investigated by constructing Fig. 6 with the micelle structural models; consequently, the micelle structure (*eg.*, N_{agg} and R_C) can become related to $M_{n,PNAT}$. This means that, once $M_{n,PNAT}$ is determined by the kinetic investigation of polymerization by eqs 1 and 6, N_{agg} and R_C are determined through the structural model

($N_{agg} = aM_{n,PNAT}^{\beta}$ and $R_C = bM_{n,PNAT}^{\gamma}$). In this way, we can calculate the time dependence of $N_{agg}(t)$ and $R_C(t)$ as the solid curves in Fig. 5, which quantitatively reproduce the experimentally-obtained data points. Here, it should be emphasized that the rate constants of the polymerization are obtained from NMR results (Fig. 3), and the time-dependence of $N_{agg}(t)$ and $R_C(t)$ are well described with these values of the rate constants.

As discussed in the introduction, we had expected that most of the macro-CTAs; thus, the active chain ends would be concentrated inside the core[27] and thus the effective local concentration of CTA and radicals may be increased. In addition, the NAT monomers may be concentrated in the core as seen in the previous work[26] or have to be transported into the core in order to react. These situations may apparently change the overall reaction rate. Besides, the increase in the effective concentration should increase the viscosity surrounding the terminal groups of polymers. It is known that this leads to much lower value of k_t. On the other hand, k_p also influenced by the viscosity, but k_p would most likely not change compared with k_t; thus, the $k_p/\sqrt{k_t}$ value should increase with the self-assembly.[28,29] In fact, for example, in the case that the core-forming block is PHPMA, higher degree of polymerization of HPMA is required to form micelles. Before and after this threshold degree of polymerization, the reaction rate significantly changed.[26]

However, contrary to expectations, we did not observe such a behaviour in the present case, as shown in Figs. 4 and 5; instead, all of the polymerizations could be explained with eq 1 having a time-independent value of $k_p/\sqrt{k_t}$. The reason can be interpreted as follows: In the present case of P(NAT-*b*-NAM) in water, even at the first frame in time-resolved SAXS (t = 5.83 min) at 70 °C in Fig. 5, where $n_{n,PNAT}$ is *ca*. 2, the micelles are already formed. That is, the effective concentration of NAT may be increased, and the overall reaction rate was accelerated by the micelle formation of P(NAT-*b*-NAM) due to the above reason at this time point. We however emphasize that this is at the very early stage ($n_{n,PNAT}$ = 2) in the present case. After the micelle formation, the effective concentration and the $k_p/\sqrt{k_t}$ value may be almost unchanged. This should be the reason why the acceleration of the polymerization in mid-course was not observed. Additionally, the low $c_{w,NAT}$ value is also related to the reaction rate. Perturbation of the polymerization kinetics may become significant when the core segment density is close to its melted state. $c_{w,NAT}$ in Fig. 8 indicates the presence of a large amount of water swelling the PNAT core. Therefore we can presume that the diffusion of the monomer (NAT) may be slowed due to the swollen core but its time scale is still shorter than that of the polymerization and no interference was observed. Furthermore, the concentration is low (c = 0.01 g/mL), compared with the previous works.[26,32] Hence, such acceleration of polymerization is possibly weak or difficult to be observed.

Conclusions

We successfully monitored the entire process of spherical micelle formation/growth through PISA by time-resolved SAXS without any appreciable beam damages, and extracted $N_{agg}(t)$ and $R_C(t)$ as functions of time. Further, the rate constants of polymerization (k_d and $k_p/\sqrt{k_t}$), and thus, the time dependence of $M_{n,PNAT}(t)$ were derived from the NMR results. The important point in the kinetic analysis for PISA is that the micellar formation/growth is much faster than the polymerization; thus, the rate-limiting process in PISA is not the micelle formation/growth *via* unimer exchange or fusion/fission but the polymerization. Hence, we were able to decouple and individually analyse the kinetics of the polymerization and the structure of micelles. Consequently, we found that a single physical principle governs the micellar formation over the entire time range and temperature even during PISA. *ie*., $M_{n,PNAT}$ is the only parameter to determine the structures regardless of the temperatures (the rate constants of polymerization) (Fig. 6). $N_{agg} \propto M_{n,PNAT}^{\beta}$ is held with the scaling exponent of β = 0.95 ± 0.05 and this relation is consistent with the de Gennes model,[43] even though it is during PISA. Moreover, by combining the kinetic model of polymerization and the structural model of micelles, the time-evolution of N_{agg}(t) and $R_C(t)$ were quantitatively described (Fig. 5).

The present case of P(NAT-*b*-NAM) in water exhibited a simple behaviour (*ie*., time-independent rate constants and the simple scaling theory well described the experimentally-obtained data). This should be because the micelle formation (thus the acceleration of the polymerization) occurs at the very early stage of $n_{n,PNAT}$ = 2. Further, we chose the spherical morphology for the simplicity to investigate the kinetics. However, our proposed analytical method may be extended to more complicated systems (*eg*., where the rate constants change in mid-course of PISA, nonspherical micelles or vesicles are formed, or PISA proceeds *via* other controlled polymerizations).

Conflicts of interest

There are no conflicts to declare.

Acknowledgements

The SAXS experiments were performed at SPring-8 under the approval of JASRI (proposal numbers: 2018A1454 and 2018B1396). This work was financially supported by JST CREST (JPMJCR1521). J. B. and F. S. further thank the DFG for generous funding in the Emmy-Noether-Program (BR 4905/3-1) and the SFB 1278 Polytarget (project A05), respectively.

References

1 S. Perrier, P. Takolpuckdee, *J. Polym. Sci. Part A,* 2005, **43,** 5347–5393.
2 S. Perrier, *Macromolecules,* 2017, **50,** 7433–7447.
3 M. R. Hill, N. R. Carmean, B. S. Sumerlin, *Macromolecules,* 2015, **48,** 5459–5469.
4 J. Kreutzer, *Nature Rev. Chem.* 2018, **2,** 0111.
5 M. Ouchi, M. Sawamoto, *Macromolecules,* 2017, **50,** 2603–2614.
6 Z. An, Q. Shi, W. Tang, C.-K. Tsung, C. J. Hawker, G. D. Stucky, *J. Am. Chem. Soc.,* 2007, **129,** 14493–14499.

7 J. T. Sun, C.-Y. Hong, C.-Y. Pan, *Soft Matter,* 2012, **8,** 7753−7767.
8 N. J. Warren, S. P. Armes, *J. Am. Chem. Soc.,* 2014, **136,** 10174−10185.
9 S. L. Canning, G. N. Smith, S. P. Armes, *Macromolecules,* 2016, **49,** 1985−2001.
10 M. Lansalot, J. Rieger, *Macromol. Rapid Commun.,* 2019, **40,** 1800885.
11 E. R. Jones, O. O. Mykhaylyk, M. Sesarilar, M. Boerakker, P. Wyman, S. P. Armes, *Macromolecules,* 2016, **49,** 172−181.
12 X. Chen, L. Liu, M. Huo, M. Zeng, L. Peng, A. Feng, X. Wang, J. Yuan, *Angew. Chem. Int. Ed.,* 2017, **56,** 16541−16545.
13 J. Tan, C. Huang, D. Liu, X. Li, J. He, Q. Xu, L. Zhang, *ACS Macro Lett.,* 2017, **6,** 298−303.
14 C. E. Boott, J. Gwyther, R. L. Harniman, D. W. Hayward, I. Manners, *Nature Chem.,* 2017, **9,** 785−792.
15 R. Deng, M. J. Derry, C. J. Mable, Y. Ning, S. P. Armes, *J. Am. Chem. Soc.,* 2017, **139,** 7616−7623.
16 M. J. Derry, O. O. Mykhaylyk, S. P. Armes, *Angew. Chem. Int. Ed.*, 2017, **56,** 1746−1750.
17 Y. Zhang, G. Han, M. Cao, T. Guo, W. Zhang, *Macromolecules,* 2018, **51,** 4397−4406.
18 J. C. Forster, S. Varlas, B. Couturaud, J. R. Jones, R. Keogh, R. T. Mathers, R. K. O'Reilly, *Angew. Chem. Int. Ed.* 2018, **57,** 15733−15737.
19 J. C. Foster, S. Varlas, B. Couturaud, Z. Coe, R. K. O'Reilly, *J. Am. Chem. Soc.,* 2019, **141,** 2742−2753.
20 Y. Ning, L. Han, J. M. Derry, F. C. Meldrum, S. P. Armes, *J. Am. Chem. Soc.,* 2019, **141,** 2557−2567.
21 F. Lv, Z. An, P. Wu, *Nature Commun.,* 2019, **10,** 1397.
22 D. Zhou, R. P. Kuchel, P. B. Zetterlund, *Polym. Chem.,* 2017, **8,** 4177−4181.
23 M. A. Touve, C. A. Figg, D. B. Wright, C. Park, J. Cantlon, B. S. Sumerlin, N. C. Gianneschi, *ACS Central Sci.,* 2018, **4,** 543−547.
24 M. J. Derry, L. A. Fielding, N. J. Warren, C. J. Mable, A. J. Smith, O. O. Mykhaylyk, S. P. Armes, *Chem. Sci.,* 2016, **7,** 5078−5090.
25 M. Alauhdin, T. M. Bennett, G. He, S. P. Bassett, G. Portale, W. Bras, D. Hermida-Merino, S. M. Howdle, *Polym. Chem.,* 2019, **10,** 860−871.
26 N. J. Warren, O. O. Mykhaylyk, D. Mahmood, A. J. Ryan, S. P. Armes, *J. Am. Chem. Soc.,* 2014, **136,** 1023−1033.
27 T. R. Guimarães, M. Khan, R. P. Kuchel, I. C. Morrow, H. Minami, G. Moad, S. Perrier, P. N. Zetterlund, *Macromolecules,* 2019, **52,** 2965−2974.
28 R. G. Gillbert, *Emulsion polymerization: a mechanistic approach;* Academic Press: New York, 1995.
29 S. C. Thickett, R. G. Gilbert, *Polymer,* 2007, **48,** 6965−6991.
30 G. Gody, T. Maschmeyer, P. B. Zetterlund, S. Perrier, *Nature Commun.,* 2013, **4,** 2505.
31 G. Gody, T. Maschmeyer, P. B. Zetterlund, S. Perrier, *Macromolecules,* 2014, **47,** 639−649.
32 F. H. Sobotta, F. Hausig, D. O. Harz, S. Hoeppener, U. S. Schubert, J. C. Brendel, *Polym. Chem.* 2018, **9,** 1593−1602.
33 H. Kurihara, S. Kitade, K. Ichino, I. Akiba, K. Sakurai, *Polym. J.,* 2019, **51,** 199−209.
34 K. Sakura, M. Takenaka, K. Tanaka, *Polym. J.,* 2019, **51,** 107.
35 D. Orthaber, A. Bergmann, O. Glatter, *J. Appl. Crystallogr.,* 2000, **33,** 218−225.
36 R. Takahashi, T. Narayanan, T. Sato, *J. Phys. Chem. Lett.,* 2017, **8,** 737−741.
37 S. J. Tseng, C.-C. Chien, Z.-X. Liao, H.-H. Chen, Y.-D. Kang, C.-L. Wang, Y. Hwu, G. Margaritondo, *Soft Matter,* 2012, **8,** 1420–1427.
38 M. H. Qiao, F. Q. Yan, W. S. Sim, J. F. Deng, G. Q. Xu, *Surf. Sci.,* 2000, **460,** 67–73.
39 O. Glatter, O. Kratky, *Small Angle X-ray Scattering*. Academic Press: London, 1982.
40 G. Gody, T. Maschmeyer, P. B. Zetterlund, S. Perrier, *Macromolecules,* 2014, **47,** 639–649.
41 R. Takahashi, T. Narayanan, S. Yusa, T. Sato, *Macromolecules,* 2018, **51,** 3654−3662.
42 J. S. Pedersen, M. C. Gerstenberg, *Macromolecules*, 1996, **29,** 1363−1365.
43 P. G. de Gennes, Macromolecules and Liquid Crystals: Reflections on Certain Lines of Research. In *Solid State Physics;* Liebert, L., Ed. Academic: New York, USA, 1978; Vol. Suppl. 14; p 1.
44 E. B. Zhulina, T. M. Birshtein, *Vysokomol. Soedin. A,* 1985, **27,** 511−517.
45 A. Halperin, *Macromolecules,* 1987, **20,** 2943−2946.
46 M. Daoud, J. P. Cotton, *J. Phys. France*, 1982, **43,** 531−538.
47 R. Nagarajan, K. Ganesh, K. *J. Chem. Phys.*, 1989, **90,** 5843−5856.
48 R. Nagarajan, K. Ganesh, K. *Macromolecules,* 1989, **22,** 4312−4325.
49 R. Nagarajan, K. Ganesh, *J. Chem. Phys.,* 1993, **98,** 7440−7450.
50 R. Nagarajan, *Adv. Colloid Interface Sci.* 2017, **244,** 113−123.
51 C. Svaneborg, J. S. Pedersen, *Macromolecules,* 2002, **35,** 1028−1037.
52 R. Koningsveld, W. H. Stockmayer, E. Nies, *Polymer Phase Diagrams: A Textbook;* Oxford University Press: Oxford, 2001.
53 H. Benoit, P. Doty, *J. Phys. Chem.,* 1953, **57,** 958−963.
54 P. J. Flory, *Principles of Polymer Chemistry;* Cornel Univ. Press: Ithaca, New York, 1953.
55 T. Sato, R. Takahashi, *Polym. J.*, 2017, **49,** 273−277.
56 R. Lund, L. Willner, D. Richter, *Adv. Polym. Sci.,* 2013, **259,** 51−158.
57 T. Sato, R. Takahashi, *Kobunshi Ronbunshu*, 2019, **76,** 3−22, in Japanese.
58 B. Bednář, K. Edwards, M. Almgren, S. Tormod, Z. Tuzar, *Makromol. Chem. Rapid Commun.,* 1988, **9,** 785−790.
59 C. Honda, Y. Hasegawa, R. Hirunuma, T. Nose, *Macromolecules,* 1994, **27,** 7660−7668.
60 E. Hecht, H. Hoffmann, *Colloid. Surf. A,* 1995, **96,** 181−197.
61 I. Goldmints, J. F. Holzwarth, K. A. Smith, T. A. Hatton, *Langmuir,* 1997, **13,** 6130−6134.
62 M. J. Kositza, C. Bohne, P. Alexandridis, T. A. Hatton, J. F. Holzwarth, *Langmuir,* 1999, **15,** 322−325.
63 G. Waton, B. Michels, R. Zena, *Macromolecules,* 2001, **34,** 907−910.
64 Z. Zhu, S. P. Armes, S. Liu, *Macromolecules,* 2005, **38,** 9803−9812.
65 Z. Zhu, J. Xu, Y. Zhou, X. Jiang, S. P. Armes, S. Liu, *Macromolecules,* 2007, **40,** 6393−6400.
66 R. Lund, L. Willner, M. Monkenbusch, P. Panine, T. Narayanan, J. Colmenero, D. Richter, *Phys. Rev. Lett.* 2009, **102,** 188301.
67 J. Kalkowski, C. Liu, P. Leon-Plata, M. Szymusiak, P. Zhang, T. Irving, W. Shang, O. Bilsel, Y. Liu, *Macromolecules,* 2019, **52,** 3151−3157.

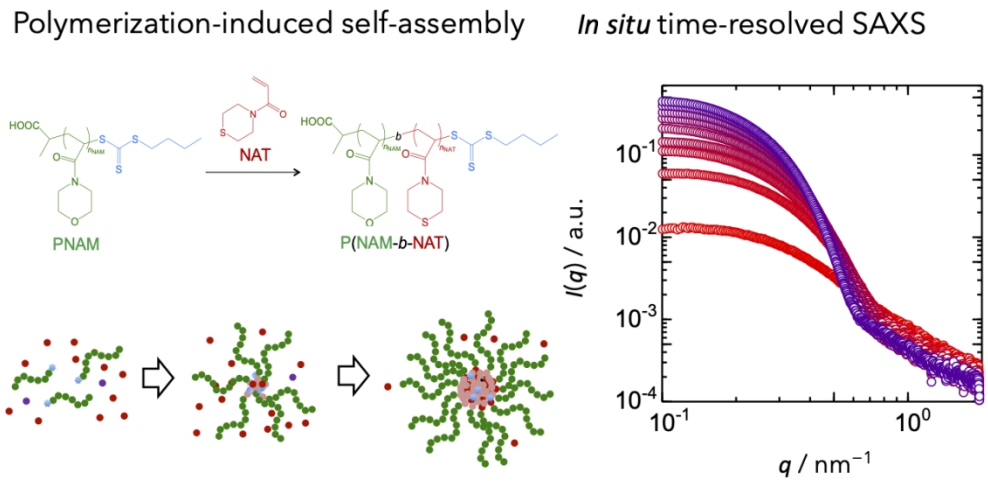

165x88mm (200 x 200 DPI)